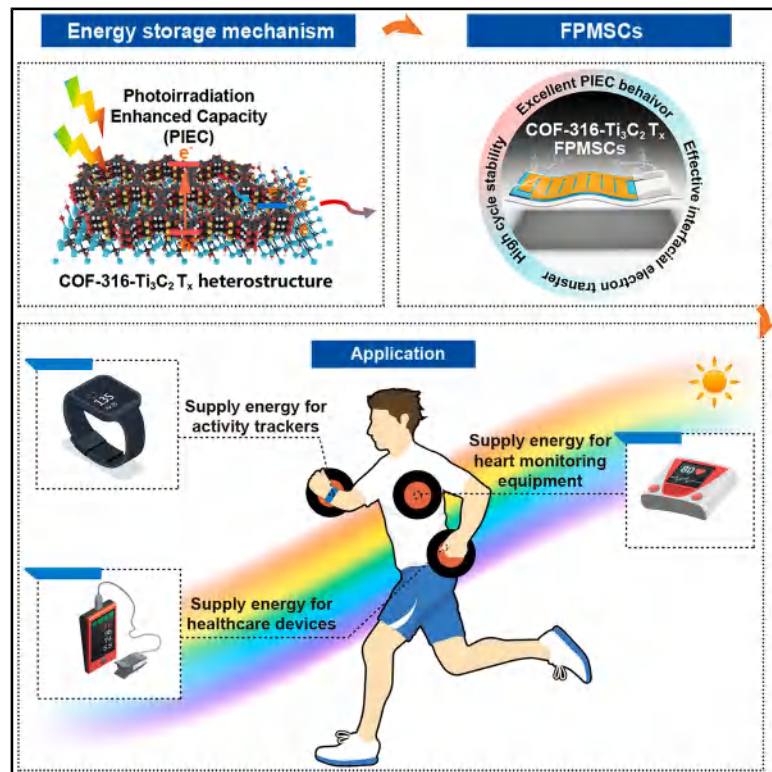


Electron-photon harvesting via built-in electric field modulation in COF/MXene heterointerfaces

Graphical abstract



Highlights

- Dynamic bonding method to fabricate core-shell COF-316-Ti₃C₂T_x heterostructure
- COF-316-Ti₃C₂T_x heterostructure prevents photoexcited charge recombination
- COF-316-Ti₃C₂T_x heterostructure improves the interfacial electron transfer efficiency
- The heterostructure endows FPMSCs with mechano-electrochemical stability

Authors

Weikang Wang (王维康), Yan Bai (白岩), Ning Ding (丁宁), ..., Mingli Liang (梁铭利), Shujuan Liu (刘淑娟), Qiang Zhao (赵强)

Correspondence

iamwwzhao@njupt.edu.cn (W.Z.), iamqzhao@njupt.edu.cn (Q.Z.)

In brief

Wang et al. present a dynamic bonding engineering strategy to synthesize core-shell COF-316-Ti₃C₂T_x heterostructures. This heterostructure prevents photoexcited charge recombination and improves the interfacial electron transfer efficiency. The COF-316-Ti₃C₂T_x FPMSCs exhibit enhanced mechano-electrochemical stability and energy storage performance under solar illumination, which highlights the feasibility of advanced heterostructures for synergistic electron-photon harvesting in flexible micro-supercapacitors.



Explore

Early prototypes with exciting performance and new methodology

Wang et al., 2025, Device 3, 100929
December 19, 2025 © 2025 Elsevier Inc. All rights are reserved, including those for text and data mining, AI training, and similar technologies.
<https://doi.org/10.1016/j.device.2025.100929>

Article

Electron-photon harvesting via built-in electric field modulation in COF/MXene heterointerfaces

Weikang Wang (王维康),^{1,3,4} Yan Bai (白岩),^{1,4} Ning Ding (丁宁),¹ Zhen You (尤振),¹ Weiwei Zhao (赵为为),^{1,*} Pin Yang (杨品),¹ Mingli Liang (梁铭利),¹ Shujuan Liu (刘淑娟),¹ and Qiang Zhao (赵强)^{1,2,5,*}

¹State Key Laboratory of Flexible Electronics (LoFE) & Jiangsu Key Laboratory for Biosensors, Institute of Advanced Materials (IAM), Nanjing University of Posts & Telecommunications, 9 Wenyuan Road, Nanjing 210023, China

²College of Electronic and Optical Engineering & College of Flexible Electronics (Future Technology), Nanjing University of Posts & Telecommunications, 9 Wenyuan Road, Nanjing 210023, China

³Institute of Rehabilitation Medicine, School of Special Education and Rehabilitation, Binzhou Medical University, 346 Guanhai Road, Yantai 264003, China

⁴These authors contributed equally

⁵Lead contact

*Correspondence: iamwwzhao@njupt.edu.cn (W.Z.), iamqzhao@njupt.edu.cn (Q.Z.)

<https://doi.org/10.1016/j.device.2025.100929>

THE BIGGER PICTURE Photo-assisted flexible supercapacitors integrate photoirradiation-enhanced capacity (PIEC) behavior, enabling increased charge storage performance under illumination for wearable electronic applications. The PIEC performance is limited by the quick recombination of photogenerated carriers, where photo-generated electrons and holes annihilate each other before participating in charge storage progress. Meanwhile, the structural instability of photoelectrodes also limits their mechano-electrochemical stability, which is attributed to poor interfacial contact and limited photochemical stability. To address these issues, this work reports a dynamic bonding engineering strategy to prepare core-shell COF-316-Ti₃C₂T_x heterostructure, which could spatially separate photo-generated carriers through built-in electric field modulation to suppress electron-hole recombination. The interface and structural integration of COF-316-Ti₃C₂T_x improve the mechano-electrochemical stability.

SUMMARY

Photo-assisted flexible supercapacitors have emerged as transformative power solutions by integrating with solar photoirradiation-enhanced capacity (PIEC) to improve energy storage performance. However, the photogenerated carrier recombination and structural instability of existing metal oxides and carbon-based photoelectrodes hinder enhancement of PIEC performance in flexible supercapacitors for wearable electronics. Herein, we propose a dynamic bonding strategy to construct a core-shell covalent organic framework/MXene heterostructure (COF-316-Ti₃C₂T_x) with engineered heterointerfaces for flexible photo-enhanced micro-supercapacitors (FPMSCs). This method facilitates the oriented growth of covalent organic framework-316 (COF-316) on a Ti₃C₂T_x nanosheet to form a core-shell heterostructure by anchoring monomers. Theoretical calculations and experiments reveal that the built-in electric field modulation accelerates photo-generated electron transfer and suppresses charge recombination (carrier lifetime is doubled). The core-shell heterostructure endows the realization of FPMSCs with enhanced mechano-electrochemical stability, including 180° bending stability and 97.5% of capacitance retention after 10,000 cycles.

INTRODUCTION

Flexible supercapacitors (FSCs) have high power density and long cycle life, yet their energy density remains constrained.^{1–5} The integration of solar energy and electrochemical storage into a single device architecture can help overcome this problem

as photoirradiation-enhanced capacity (PIEC) behavior can generate photocarriers that activate redox reactions and mitigate ion diffusion limitations.^{6,7} For instance, Ding et al. have fabricated Cu@Cu₂O hybrid arrays with PIEC behavior to achieve 37.9% increased capacitance under light illumination than that in the dark, which is ascribed to the photogenerated

holes-assisted faradaic reaction between Cu_2O and CuO for enhanced pseudocapacitive activity.⁸ Zhang et al. have fabricated a $\text{Co}_3\text{O}_4/\text{g-C}_3\text{N}_4$ p-n junction to prepare photocatalysis-assisted supercapacitors with 83.3% capacity retention after 5,000 galvanostatic charge/discharge (GCD) cycles. This is attributed to that the photogenerated carriers of $\text{Co}_3\text{O}_4/\text{g-C}_3\text{N}_4$ p-n junction that can participate in the pseudocapacitive reactions of Co_3O_4 and CoO_2 during charge-discharging processes.⁹ Despite these achievements, there are still challenges to raise the areal capacitance (C_A) and long-term life of flexible photoirradiation-enhanced micro-supercapacitors (FPMSCs), due to the severe photogenerated carrier recombination, structural instability under bending, and limited light absorption window, which hinder applications.

As a class of organic porous crystalline materials, covalent organic framework (COF) is comprised of organic building blocks linked by covalent bonds, which have promising applications in drug delivery,¹⁰ catalysis,^{11,12} and energy storage,^{13,14} due to the high crystallinity, abundant reactive sites, and large specific surface areas.^{15,16} Moreover, the structural characteristics with rigid π -conjugated units and structural adjustability exhibit versatile photoelectric functionalization and energy storage property,^{17,18} which endow COF with application potential in the field of PIEC micro-supercapacitors. However, the low conductivity and charge recombination issues of COF materials hinder the improvement of their optoelectronic performance.^{19,20} Reasonable composite structure design presents a promising strategy to accelerate charge-carrier separation during the light irradiation process.²¹ As a two-dimensional (2D) transition metal carbides, nitrides, and carbonitrides materials, MXene possesses abundant terminal groups ($-\text{F}$, $-\text{O}$, and $-\text{OH}$), which is beneficial to fabricate hybrids via electrostatic absorption or intercalation.^{22–24} It exhibits metallic conductivity, hydrophilicity, and large surface area, making it a promising material for energy storage applications.²⁵ However, MXene with thermodynamically metastable surfaces tends to be oxidized under ambient conditions, which is detrimental to the structural stability and energy storage performance.^{26,27} Surface encapsulation of MXene nanosheets is a strategy to enhance antioxidant capacity by restricting contact of oxygen with MXene nanosheets.²⁸ The built-in electric field (BIEF) at the heterojunction interface can promote the separation of photogenerated carriers.²⁹

Herein, we developed a dynamic bonding engineering approach to construct core-shell COF-316- $\text{Ti}_3\text{C}_2\text{T}_x$ heterostructure with interfacial charge transfer and mechanically reinforced architecture for high-performance FPMSCs. The transformation mechanism is based on the surface-initiated dynamic hydrogen bonding anchoring of 2,3,6,7,10,11-hexahydroxytriphenylene (HHTP) monomers to facilitate the oriented growth of COF-316 on the surface of $\text{Ti}_3\text{C}_2\text{T}_x$ nanosheets for the formation of core-shell COF-316- $\text{Ti}_3\text{C}_2\text{T}_x$ heterostructure. The as-produced BIEF modulation in COF-316- $\text{Ti}_3\text{C}_2\text{T}_x$ heterostructure prevents the photoexcited charge recombination and extends carrier lifetime by two times to enhance the PIEC behavior under light illumination. It improves the interfacial electron transfer efficiency from COF-316 to $\text{Ti}_3\text{C}_2\text{T}_x$ as evidenced by transient photocurrent analysis and theoretical calculations. The C_A of COF-316- $\text{Ti}_3\text{C}_2\text{T}_x$ FPMSCs reaches 2.44 mF cm^{-2} under light illumination,

which is 47.8% higher than that in dark. Furthermore, the COF-316- $\text{Ti}_3\text{C}_2\text{T}_x$ heterostructure improves the antioxidant and structural stability of $\text{Ti}_3\text{C}_2\text{T}_x$ nanosheets to enhance the mechano-electrochemical stability. The COF-316- $\text{Ti}_3\text{C}_2\text{T}_x$ FPMSCs exhibit bending stability of 180° and capacitance retention performance of 97.5% after 10,000 charge-discharge cycles.

RESULTS AND DISCUSSION

Design and fabrication of core-shell COF-316- $\text{Ti}_3\text{C}_2\text{T}_x$ nanosheets

In this work, core-shell COF-316- $\text{Ti}_3\text{C}_2\text{T}_x$ nanosheets are fabricated via prior dynamic bonding of HHTP organic ligands on the $\text{Ti}_3\text{C}_2\text{T}_x$ substrates (Figures 1A, S1, and S2). Scanning electron microscopy (SEM) and transmission electron microscopy (TEM) images demonstrate that the COF-316- $\text{Ti}_3\text{C}_2\text{T}_x$ heterostructure possesses characteristic 2D nanosheet structures with rough surfaces (Figures 1B and 1C), attributed to the uniform growth of COF-316 on the surface of $\text{Ti}_3\text{C}_2\text{T}_x$ nanosheets. A high-resolution TEM (HRTEM) image shows that the spacing of lattice fringes of COF-316- $\text{Ti}_3\text{C}_2\text{T}_x$ nanosheets are 0.21 nm and 0.33 nm, respectively (Figure 1C), which corresponds to the (111) lattice plane of $\text{Ti}_3\text{C}_2\text{T}_x$ nanosheets and the (101) lattice plane of COF-316.³⁰ Moreover, the reticular structure with hexagonal pores is also observed on the surface of COF-316- $\text{Ti}_3\text{C}_2\text{T}_x$ nanosheets, which matches well with the topology of COF-316. Energy-dispersive X-ray spectroscopy analysis shows that the signals of C, Ti, O, and N elements are uniformly distributed over COF-316- $\text{Ti}_3\text{C}_2\text{T}_x$ nanosheets (Figure 1D), which implies a homogeneous construction of COF-316 and $\text{Ti}_3\text{C}_2\text{T}_x$ nanosheets.

Powder X-ray diffraction (PXRD) demonstrates the diffraction peaks at 4.4° and 26.9° of COF-316- $\text{Ti}_3\text{C}_2\text{T}_x$ nanosheets corresponding to the COF-316 lattice planes of (100) and (001), are matched well with the lattice fringes (Figures 1E and S4).³¹ Compared with $\text{Ti}_3\text{C}_2\text{T}_x$, the PXRD peak of COF-316- $\text{Ti}_3\text{C}_2\text{T}_x$ nanosheets downshifts from 6.5° to 6.1° , which indicates the structure stability of $\text{Ti}_3\text{C}_2\text{T}_x$ and the increase of the interlayer spacing from 1.36 nm for $\text{Ti}_3\text{C}_2\text{T}_x$ to 1.45 nm for COF-316- $\text{Ti}_3\text{C}_2\text{T}_x$. It is attributed to the fact that the formation of core-shell COF-316- $\text{Ti}_3\text{C}_2\text{T}_x$ heterostructure increases the interlayer spacing of $\text{Ti}_3\text{C}_2\text{T}_x$ nanosheets. The Brunauer-Emmett-Teller method reveals that COF-316- $\text{Ti}_3\text{C}_2\text{T}_x$ nanosheets exhibit a specific surface area of $154.68 \text{ m}^2 \text{ g}^{-1}$, which is an order of magnitude greater than that of $\text{Ti}_3\text{C}_2\text{T}_x$ nanosheets ($17.93 \text{ m}^2 \text{ g}^{-1}$) (Figure 1F). The increase in specific surface area is caused by the uniform coverage of COF-316 on the surface of Ti_3C_2 nanosheets, which engenders a proliferation of contact sites. This structural evolution establishes the foundation for substantially improved energy storage performance. Compared with pristine $\text{Ti}_3\text{C}_2\text{T}_x$, the Fourier-transform infrared (FTIR) spectra of COF-316- $\text{Ti}_3\text{C}_2\text{T}_x$ nanosheets exhibits new adsorption peaks at $1,150$ – $1,680$, $1,268$, and $2,240 \text{ cm}^{-1}$, corresponding to aromatic rings, $\text{C}=\text{O}$, and $-\text{CN}$ functional groups, respectively (Figure 1G).³² It indicates that the organic ligands have successfully reacted and integrated with $\text{Ti}_3\text{C}_2\text{T}_x$ to form the COF-316- $\text{Ti}_3\text{C}_2\text{T}_x$ nanosheets. The decreased intensity of the absorption peaks at $3,400 \text{ cm}^{-1}$ for $-\text{OH}$ groups confirms that the COF-316- $\text{Ti}_3\text{C}_2\text{T}_x$ nanosheets are involved in

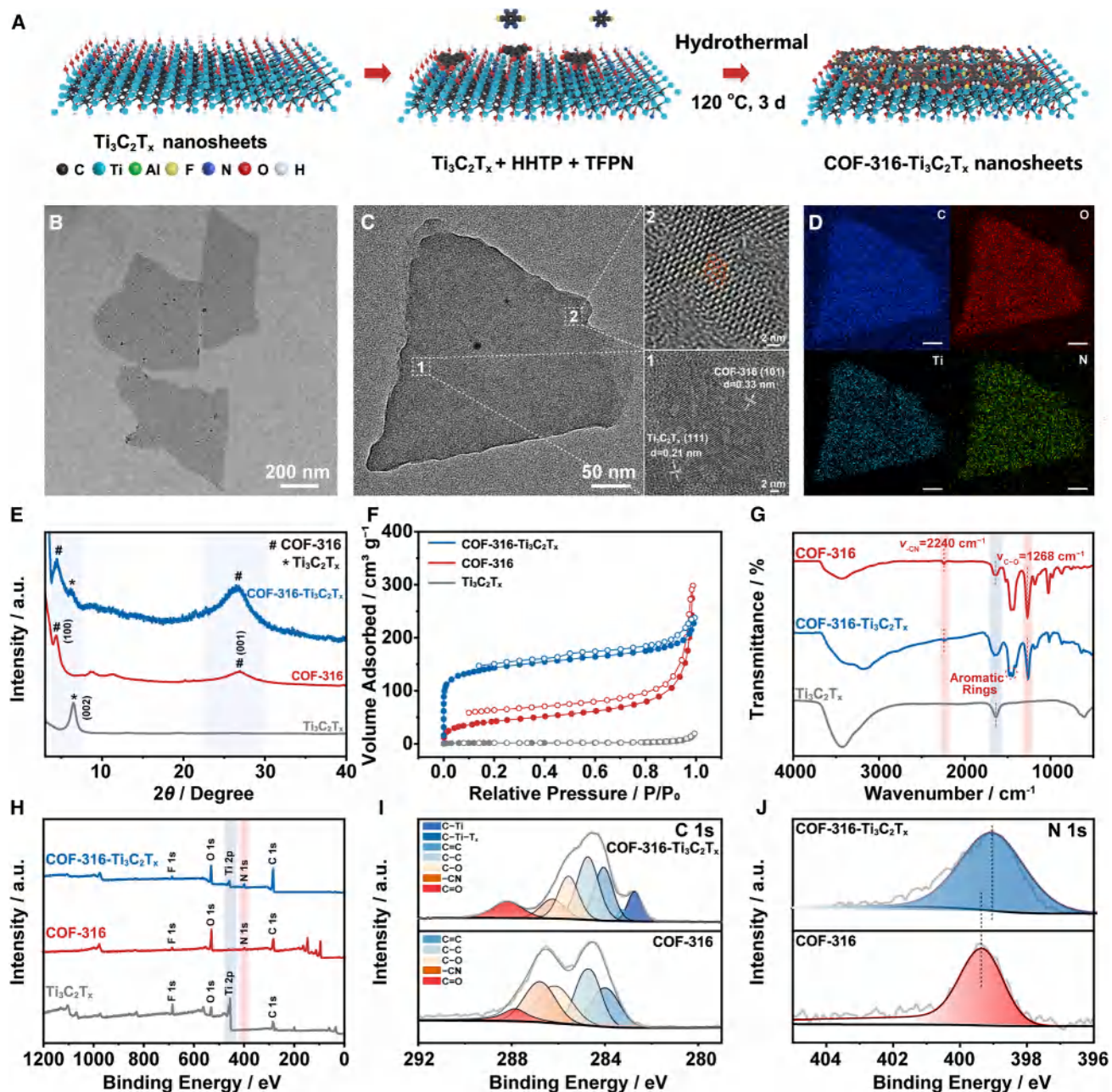


Figure 1. Characterization of core-shell COF-316-Ti₃C₂T_x nanosheets

(A) Synthesis diagram of the synthesis process of COF-316-Ti₃C₂T_x.

(B and C) TEM images of Ti₃C₂T_x nanosheets (B) and COF-316-Ti₃C₂T_x (C), with panels 1 and 2 showing enlarged lattice regions to highlight surface structural details.

(D) Elemental mapping images of COF-316-Ti₃C₂T_x, demonstrating uniform distribution of key elements (scale bar: 50 nm).

(E) XRD patterns of COF-316-Ti₃C₂T_x, confirming the crystallinity and structural features of the composite.

(F) N₂ adsorption and desorption isotherms, revealing the surface area and porosity of COF-316-Ti₃C₂T_x.

(G) FTIR spectra of COF-316-Ti₃C₂T_x, indicating characteristic functional groups and successful integration.

(H–J) XPS spectra (H) and high-resolution spectra of C 1s (I) and N 1s (J), providing insight into the chemical composition and bonding states of the heterostructure.

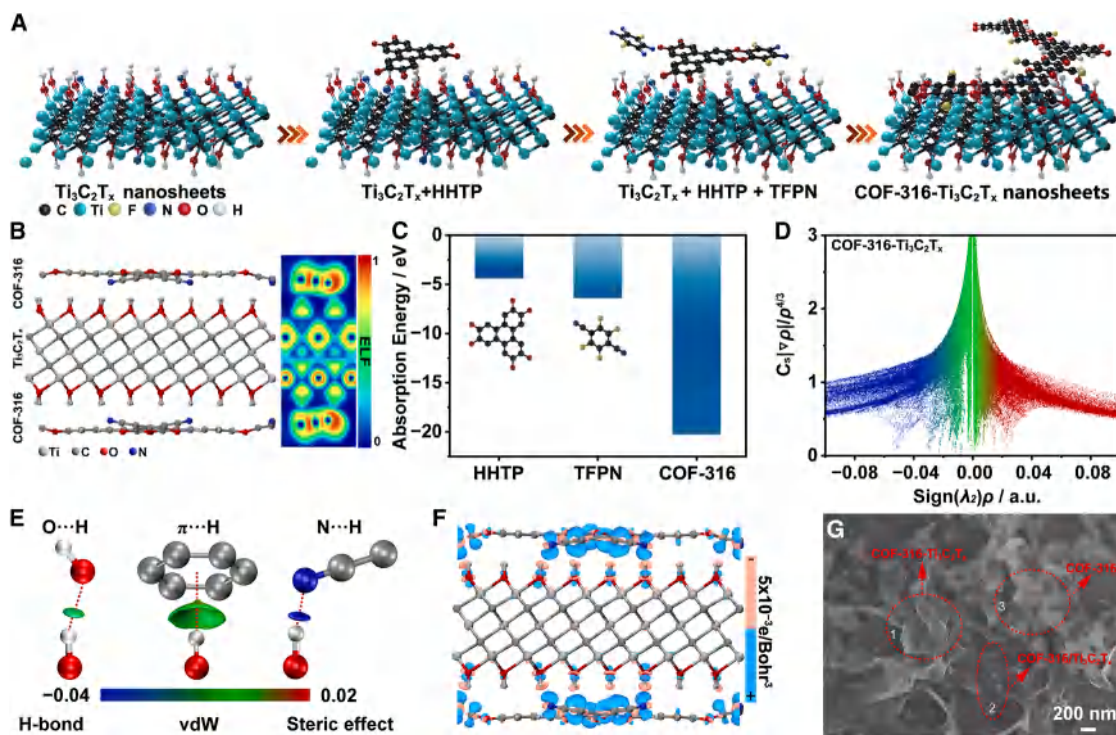


Figure 2. Evolution mechanism of COF-316- $\text{Ti}_3\text{C}_2\text{T}_x$ heterostructures

- (A) Schematic illustration of the formation process.
- (B) Optimized geometric configuration of $\text{COF-316}-\text{Ti}_3\text{C}_2\text{T}_x$ heterojunctions (left) with electron localization function (ELF) mappings (right), highlighting regions of electron accumulation at the interface.
- (C) E_{ad} between $\text{Ti}_3\text{C}_2\text{T}_x$ and different absorbing units (HHTP, TFPN, and COF-316), showing the relative interaction strengths.
- (D) $\text{Sign}(\lambda_2)\rho$ mapped 2D scatterplot of the reduced electron density gradient $s = C_s |\nabla \rho| / \rho^{4/3}$ of $\text{COF-316}-\text{Ti}_3\text{C}_2\text{T}_x$ junctions, providing insight into non-covalent interactions at the junction.
- (E) The corresponding isosurfaces of $s = 0.5$, which include the non-covalent interactions between $-\text{OH}$ groups on the $\text{Ti}_3\text{C}_2\text{T}_x$ surface and different chemical groups (phenolic hydroxyl groups, conjugated aromatic structure, and $-\text{CN}$). The isosurfaces are colored on a blue-green-red scale according to values of $\text{sign}(\lambda_2)\rho$ (-0.04 to 0.02 a.u.) to indicate interaction strength.
- (F) Electron density difference mapping ($\Delta\rho$) between COF-316 and $\text{Ti}_3\text{C}_2\text{T}_x$, highlighting charge transfer behavior at the interface. $\Delta\rho$ is calculated by $\Delta\rho = \rho_{s-m} - \rho_s - \rho_m$, where ρ_{s-m} , ρ_s , and ρ_m are the electron density of the junction, semiconductor, and metal, respectively.
- (G) SEM image of the product by changing the order of monomer addition, illustrating the impact of synthetic sequence on structural evolution.

hydrogen bonding interaction between COF-316 and $\text{Ti}_3\text{C}_2\text{T}_x$ nanosheets. Thermogravimetric analysis illustrates that the thermal stability is similar to that of COF-316 up to 440°C without significant weight loss, which proves the preparation of the composite nanosheets (Figure S5).³³

The high-resolution X-ray photoelectron spectroscopy (XPS) is measured to gain a better understanding of the heterostructure. N atoms are detected in the XPS survey of COF-316- $\text{Ti}_3\text{C}_2\text{T}_x$, confirming the presence of $-\text{CN}$ groups on the $\text{Ti}_3\text{C}_2\text{T}_x$. The high-resolution XPS confirms that C, O, Ti, F, and N atoms are distributed in COF-316- $\text{Ti}_3\text{C}_2\text{T}_x$ nanosheets (Figures 1H–J).³⁴ The emergence of the C=C groups at 284.1 eV and the enhanced intensity of C-C, C-O, and C=O groups at 284.8, 285.4, and 288.4 eV indicate the existence of aromatic groups in C 1s XPS spectra, which is attributed to the existence of COF-316 in C 1s XPS spectra, the binding energy of the $-\text{CN}$ group (286.4 eV) has a slight negative shift of 0.4 eV compared with COF-316 (286.8 eV). It can be explained by the fact that the COF-316- $\text{Ti}_3\text{C}_2\text{T}_x$ heterostructure, formed through

hydrogen-bond interactions, modifies the interfacial charge distribution to increase the electron density around the $-\text{CN}$ groups. The enhanced electron density could increase the electronic shielding of $-\text{CN}$ groups, which reduces the effective nuclear attraction on the valence electrons and consequently decreases the binding energy.³⁵ In the N 1s XPS spectra, the binding energy of the $-\text{CN}$ group (399.1 eV) has a similar negative shift of 0.3 eV compared with COF-316 (399.4 eV), which proves that the hydrogen bonding interaction between the $-\text{CN}$ group and $\text{Ti}_3\text{C}_2\text{T}_x$ provides a bridge for interface charge transfer. The cumulative evidence substantiates the successful fabrication of core-shell COF-316- $\text{Ti}_3\text{C}_2\text{T}_x$ heterostructure, wherein hydrogen bonding interaction serves as the key driving force to promote the growth of COF-316 on the surface of $\text{Ti}_3\text{C}_2\text{T}_x$ nanosheets.

Formation mechanism of core-shell COF-316- $\text{Ti}_3\text{C}_2\text{T}_x$ heterostructure

To understand the formation mechanism of core-shell heterostructure, we investigate the formation mechanism of

COF-316-Ti₃C₂T_x (Figure 2A). Theoretical calculation serves as an effective approach to explore the electronic property and dynamic bonding engineering of COF-316-Ti₃C₂T_x heterostructure (Figures 2B and S6). The electron local function mappings reveal interfacial regions with moderate electron localization ($\eta \approx 0.35\text{--}0.45$) between COF-316 and Ti₃C₂T_x, which are spatially correlated with donor-acceptor atomic pairs (N ... H–O). This finding confirms the formation of a heterostructure induced by hydrogen bonding. Ti₃C₂T_x nanosheets, rich in terminal –OH groups, can interact with the phenolic hydroxyl groups and conjugated aromatic structure in HHTP, leading to the formation of a uniformly distributed HHTP layer. To elucidate the bond order changes and the local electron distribution of H atoms in phenolic hydroxyl groups, the Mayer bond order and minimal basis iterative stockholder charge are calculated. This enables a better understanding of the impact of hydrogen bonding interactions on the formation of pre-activated HHTP. The hydrogen bonding interactions alter the charge distribution of phenolic hydroxyl groups, enhancing their reactivity and resulting in the formation of pre-activated HHTP. Compared with HHTP, the phenolic hydroxyl groups of HHTP-Ti₃C₂T_x exhibit a smaller Mayer bond order (~2.3%) and minimal basis iterative stockholder charge (~5.5%) (Table S1). This suggests that the hydrogen bonding between the phenolic hydroxyl groups of HHTP and the terminal –OH groups of Ti₃C₂T_x nanosheets facilitates the reduction of bond order and deprotonation of phenolic hydroxyl groups, which is crucial for the formation of the pre-activated HHTP-Ti₃C₂T_x layer. The pre-activated HHTP anchored on the Ti₃C₂T_x surface preferentially undergoes a nucleophilic substitution reaction with tetrafluorophthalonitrile (TFPN) to form C–O–C linkages, followed by further defluorination to synthesize an oriented COF-316 layer.

Moreover, the adsorption energy (E_{ad}) of the smallest repeating unit of COF-316 (~20.31 eV) is lower than that of HHTP (~4.47 eV) and TFPN (~6.44 eV) (Figures 2C and S7).³⁶ It indicates that COF-316, with its abundant –CN groups and conjugated aromatic structures, can interact with the –OH groups on the surface of Ti₃C₂T_x through stronger hydrogen bonds and π - π stacking interactions, thereby generating the COF-316-Ti₃C₂T_x heterostructure. To assess the influence of dynamic bonding engineering on the formation of the core-shell COF-316-Ti₃C₂T_x heterostructure, the non-covalent interactions between the –OH groups on the surface of Ti₃C₂T_x and different chemical groups (i.e., phenolic hydroxyl groups, conjugated aromatic structure, and –CN) are analyzed using the reduced density gradient model.³⁷ Compared with HHTP-Ti₃C₂T_x, stronger hydrogen bonding and π - π stacking interactions are formed at the COF-316-Ti₃C₂T_x interface, which contributes to the formation of a stable COF-316-Ti₃C₂T_x heterostructure (Figures 2D and S8). The sign(λ_2)_p value for –CN groups is higher than that for –OH groups and phenolic hydroxyl groups, indicating stronger hydrogen bonding between the –CN groups and the –OH groups on the surface of Ti₃C₂T_x (Figure 2E). It demonstrates the significance of dynamic bonding engineering in the formation of the core-shell COF-316-Ti₃C₂T_x heterostructure. The core-shell heterostructure of COF-316-Ti₃C₂T_x indicates that COF-316 undergoes oriented growth with a planar configuration on Ti₃C₂T_x to construct a COF network structure.

The electron density difference is calculated to illustrate the interface charge transfer and gain a deeper understanding of the charge transfer process in multiple interface structures (Figure 2F).³⁸ In the electron density maps, the red and blue iso-surfaces represent regions of charge accumulation and deficit, respectively. Charges tend to accumulate at the interface between the –CN groups and the –OH groups on the surface of Ti₃C₂T_x. It suggests that the COF-316-Ti₃C₂T_x heterostructure based on hydrogen bonding interactions can modify the charge distribution and induce an imbalance in the interface charge distribution. As a result, a BIEF is formed at the heterogeneous interface, directed from Ti₃C₂T_x to COF-316, which enhances the interface electron charge transfer efficiency from COF-316 to Ti₃C₂T_x (Figure S9).

To explore the influence of dynamic bonding engineering on the formation of the core-shell COF-316-Ti₃C₂T_x heterostructure, the addition order of monomers is investigated. It is difficult to synthesize the core-shell heterostructure when the addition order of HHTP and TFPN is exchanged (Figure 2G). This phenomenon is primarily attributed to the fact that the hydrogen-bonding interaction between TFPN and the terminal groups on the Ti₃C₂T_x surface is achieved through the –CN group and the π -electron cloud of the conjugated aromatic structure, which has no activating effect on the –F of TFPN. HHTP can simultaneously undergo nucleophilic aromatic substitution reactions with TFPN in the solution and anchor on the surface of Ti₃C₂T_x, leading to the synthesis of phase-separated COF-316-Ti₃C₂T_x (PS COF-316-Ti₃C₂T_x) structures between the Ti₃C₂T_x nanosheets and spherical COF-316. Moreover, a blank control experiment is conducted. In this experiment, only Ti₃C₂T_x nanosheets are subjected to hydrothermal treatment without the addition of HHTP and TFPN monomers. During this process, the Ti₃C₂T_x nanosheets show obvious cleavage and oxidation, accompanied by the generation of TiO₂ (Figure S10). These results indicate that both the surface anchoring and pre-activation of HHTP in the dynamic bonding engineering strategy are equally crucial for the formation of the core-shell COF-316-Ti₃C₂T_x heterostructure. The preferential reaction between the pre-activated HHTP anchored on the surface of the Ti₃C₂T_x nanosheets and TFPN drives the oriented growth of COF-316, enabling the synthesis of the core-shell heterostructure. The oriented COF-316 layers, rich in –CN groups and conjugated aromatic structures, interact with the –OH groups on the surface of Ti₃C₂T_x through stronger hydrogen bonding and π - π stacking interactions to generate the COF-316-Ti₃C₂T_x heterostructure. The COF-316 strongly anchored on the surface acts as an antioxidant to protect Ti₃C₂T_x.

Electrochemical and antioxidant performance of the core-shell COF-316-Ti₃C₂T_x nanosheets

To explore the impact of COF-316-Ti₃C₂T_x heterostructure and PIEC behavior on electrochemical performance, electrodes made of Ti₃C₂T_x, COF-316, COF-316-Ti₃C₂T_x, and physically mixed COF-316-Ti₃C₂T_x (COF-316-Ti₃C₂T_x-PM) are separately tested using a three-electrode configuration. The tests are conducted in a 0.5 M H₂SO₄ electrolyte within a potential window ranging from –0.2 to 0.4 V (vs. Ag/AgCl), under both dark and light illumination conditions (Figures S11–S13). The energy

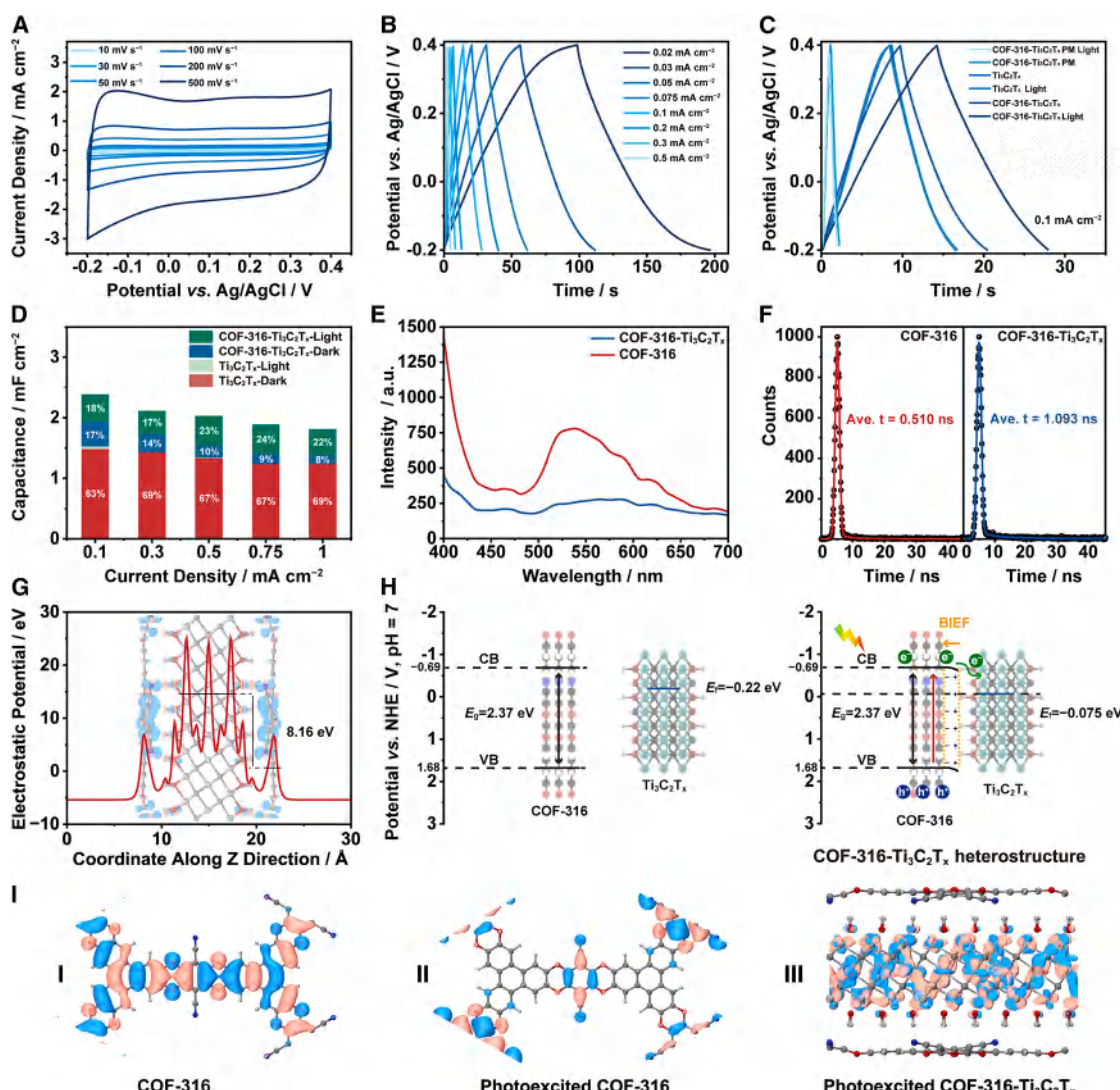


Figure 3. The electrochemical characterization of COF-316-Ti₃C₂T_x electrode

- (A) CV curves at different scan rates.
- (B) GCD curves at different current densities, highlighting charge-discharge performance and rate capability.
- (C) GCD curves at 0.1 mA cm⁻² under light illumination and dark conditions, showing the PIEC behavior.
- (D) C_a of COF-316, Ti₃C₂T_x, and COF-316-Ti₃C₂T_x electrodes at different current densities, illustrating comparative charge storage performance.
- (E) Steady-state photoluminescent spectra of COF-316 and COF-316-Ti₃C₂T_x, revealing photoinduced carrier recombination behavior.
- (F) Transient absorption decay profiles of COF-316 and COF-316-Ti₃C₂T_x, providing insights into carrier lifetimes and charge transfer dynamics.
- (G) Calculated planar averaged electrostatic potential along z axis (insert: the electron density difference mapping between COF-316 and Ti₃C₂T_x), highlighting interfacial charge redistribution.
- (H) Energy band alignment diagrams for metallic Ti₃C₂T_x and semiconductor COF-316 before and after Schottky contact.
- (I) Distinct electronic states: (I) COF-316, (II) photoexcited COF-316, and (III) charge accumulation at E_f of photoexcited COF-316-Ti₃C₂T_x, indicating photoinduced charge separation at the heterojunction.

storage performance of the COF-316-Ti₃C₂T_x electrode is evaluated by cyclic voltammetry (CV) at different scan rates from 10 to 500 mV s⁻¹ (Figure 3A). The distinct symmetric pseudo-rectangular shape with a broad redox peak indicates that the COF-316-Ti₃C₂T_x electrode has high reversibility in the charge/discharge process. It combines the energy storage behaviors of pseudocapacitance and electric double-layer capacitance. The incorporation of COF-316, which is rich in reactive sites

and has an aromatic conjugated structure, is conducive to enhancing both pseudocapacitance and electric double-layer capacitance.³⁹ The GCD curves reveal good symmetry and a triangular shape with slight linear deviation, demonstrating that COF-316-Ti₃C₂T_x electrode exhibits energy storage characteristics, which is consistent with the CV curves (Figure 3B). The COF-316-Ti₃C₂T_x electrode exhibits a high-rate capability of 73.3% and high Coulombic efficiency under the current density

increases from 0.1 mA cm^{-2} to 1 mA cm^{-2} (Figures S14A and S14B). Meanwhile, the rate capability and Coulomb efficiency of COF-316-Ti₃C₂T_x electrode also exhibit good stability under light illumination and dark conditions. Under light illumination at a current density of 0.1 mA cm^{-2} , the C_A of COF-316-Ti₃C₂T_x electrode reaches 2.33 mF cm^{-2} , which is 51.2% higher than that of the Ti₃C₂T_x electrode (1.54 mF cm^{-2}) and 22.0% higher than that of the COF-316-Ti₃C₂T_x electrode in the dark (1.91 mF cm^{-2}) (Figures 3C, 3D, and S15).

To reflect the influence of core-shell COF-316-Ti₃C₂T_x heterostructure on electrochemical performance, the PS COF-316-Ti₃C₂T_x are measured using a three-electrode configuration (Figure S16). The C_A of COF-316-Ti₃C₂T_x electrode (1.91 mF cm^{-2}) is higher than that of PS COF-316-Ti₃C₂T_x (0.2 mF cm^{-2}). This improvement is ascribed to the fact that the COF-316-Ti₃C₂T_x composites consist of ultra-thin COF-316 layers grown *in situ* on the surface of Ti₃C₂T_x nanosheets, which allows for the full exposure of reactive sites.⁴⁰ Moreover, the COF-316-Ti₃C₂T_x electrode, with its PIEC effect, generates a larger number of photogenerated charges under light illumination. The uneven electron distribution between COF-316 and Ti₃C₂T_x nanosheets creates a BIEF at the heterointerface, which accelerates charge transport and suppresses charge recombination, which is consistent with the electron density maps (Figure 2F).⁴¹

To understand the mechanism of PIEC behavior in the COF-316-Ti₃C₂T_x electrode, the photophysical properties and band gaps are explored. In comparison with COF-316, COF-316-Ti₃C₂T_x shows photoluminescence (PL) quenching at 540 nm in the steady-state PL spectra, which indicates that the composite heterojunction facilitates the non-radiative energy transfer of photogenerated carriers (Figure 3E). Additionally, COF-316-Ti₃C₂T_x has an evidently longer average emission lifetime (1.093 ns) than COF-316 (0.510 ns) (Figure 3F). The PL quenching and the prolonged excited state confirm the establishment of charge transfer between COF-316 and Ti₃C₂T_x. It suppresses the recombination of photoexcited charges and enhances non-radiative energy transfer, improving the PIEC behavior.^{21,42} The enhanced electrochemical performance of COF-316-Ti₃C₂T_x is validated by first-principles density functional theory. The average electrostatic potential (AESP) of Ti₃C₂T_x (7.25 eV) is higher than that of COF-316 (-0.91 eV), suggesting that electrons migrate from COF-316 to Ti₃C₂T_x under the BIEF (Figure 3G).⁴³ The energy band alignment diagrams in Figure 3H provide in-depth insights into the mechanism of PIEC behavior in the COF-316-Ti₃C₂T_x heterostructure. The optical band gap of COF-316 is calculated to be 2.37 eV through Tauc-plot analysis of its solid-state UV-vis absorption spectra (Figure S17).⁴⁴ The conduction band (CB) and valence band (VB) of COF-316 are determined to be -0.69 and 1.68 eV , respectively (Figures 3I and S18).⁴⁵ Fermi level (E_F) of Ti₃C₂T_x, located at -0.22 eV , is calculated with the local vacuum level set to zero.⁴⁶ Due to the difference in E_F , free electrons spontaneously migrate from the metallic Ti₃C₂T_x side to the semiconductor COF-316 side upon contact until E_F equilibrium is reached. This is consistent with the electron migration observed in the electron density difference analysis and the energy level shift in the density of states analysis (Figures S19 and S20). The directional electron transfer generates a BIEF and a contin-

uous electron flow at the Mott-Schottky heterojunction interface. This drives the rapid migration of photogenerated electrons from the CB of COF-316 to the Ti₃C₂T_x, enabling efficient charge separation. In summary, theoretical calculations and photophysical analysis demonstrate that the BIEF at the COF-316-Ti₃C₂T_x interface promotes the transfer of photogenerated electrons and effectively inhibits the recombination of photogenerated carriers during the energy storage process.

To prove the antioxidant performance of COF-316-Ti₃C₂T_x nanosheets, the structural stability is investigated in air atmosphere. After air exposure for 3 weeks, TEM images show that COF-316-Ti₃C₂T_x nanosheets maintain 2D nanosheets, which demonstrates morphology stability (Figures 4A and 4B). In comparison, Ti₃C₂T_x nanosheets exhibit obvious degradation, with spindles and rod-like TiO₂ nanoparticles dispersed on the surface and edges of the COF-316-Ti₃C₂T_x after 3 weeks. Moreover, Ti 2p XPS spectra confirm that there is no significant change in the characteristic peaks (Figure 4C). The relative atomic percentages are 9.8%, 21.1%, 49.2%, and 19.9% for Ti-C, Ti²⁺, Ti³⁺, and Ti⁴⁺ species, respectively, which shows negligible variation in the COF-316-Ti₃C₂T_x after 3 weeks (Figures 4D and S21 and Table S2). In comparison, Ti₃C₂T_x nanosheets exhibit obvious degradation, in which the relative atomic percentages of Ti⁴⁺ at 459.0 eV increase from 15.5% to 23.6%. The attachment of O₂ and H₂O molecules to Ti₃C₂T_x is the key reason for the oxidation phenomenon.

We have calculated the E_{ad} of O on the surface of Ti₃C₂T_x and COF-316-Ti₃C₂T_x nanosheets.³⁶ Compared with the E_{ad} (-10.04 eV) of the oxygen site of Ti₃C₂T_x, the E_{ad} of the N site of COF-316-Ti₃C₂T_x nanosheets obviously decreases to -6.51 eV (Figures 4E and 4F). It proves that the COF-316-Ti₃C₂T_x heterostructure reduces the E_{ad} of O on the surfaces of Ti₃C₂T_x and improves the antioxidant structural stability of Ti₃C₂T_x nanosheets. The enhanced structural stability endows the electrode with capacitance retention. The C_A of the COF-316-Ti₃C₂T_x electrode reaches 1.54 mF cm^{-2} at 0.1 mA cm^{-2} , which is three times higher than that of the Ti₃C₂T_x electrode (0.48 mF cm^{-2}) after 3 weeks. Moreover, compared with pure Ti₃C₂T_x (32.3%), the capacitance retention of COF-316-Ti₃C₂T_x can reach 80.5% after oxidation for 3 weeks (Figures 4G and 4H). This supports that the heterostructure can improve the antioxidant stability of Ti₃C₂T_x nanosheets and exhibit capacitance retention through oxidation measurement for 3 weeks. Consequently, the core-shell heterostructure can be engineered through the steric shielding of COF-316. A comparative radar map illustrates the advantages of COF-316-Ti₃C₂T_x over Ti₃C₂T_x and COF-316 in terms of C_A and PIEC behavior (Figure 4I). The heterostructure concurrently suppresses the recombination of photogenerated carriers, accelerates interfacial charge transfer, and enhances structural stability to improve PIEC behavior during the energy storage process (Figure 4J).

Fabrication and characterization of COF-316-Ti₃C₂T_x FPMSCs

The COF-316-Ti₃C₂T_x FPMSCs have been prepared by the microelectronic printer, in which COF-316-Ti₃C₂T_x is used as active electrode materials, silver paste as the conductive substrate, and polyvinyl alcohol (PVA)/H₂SO₄ gels as electrolyte

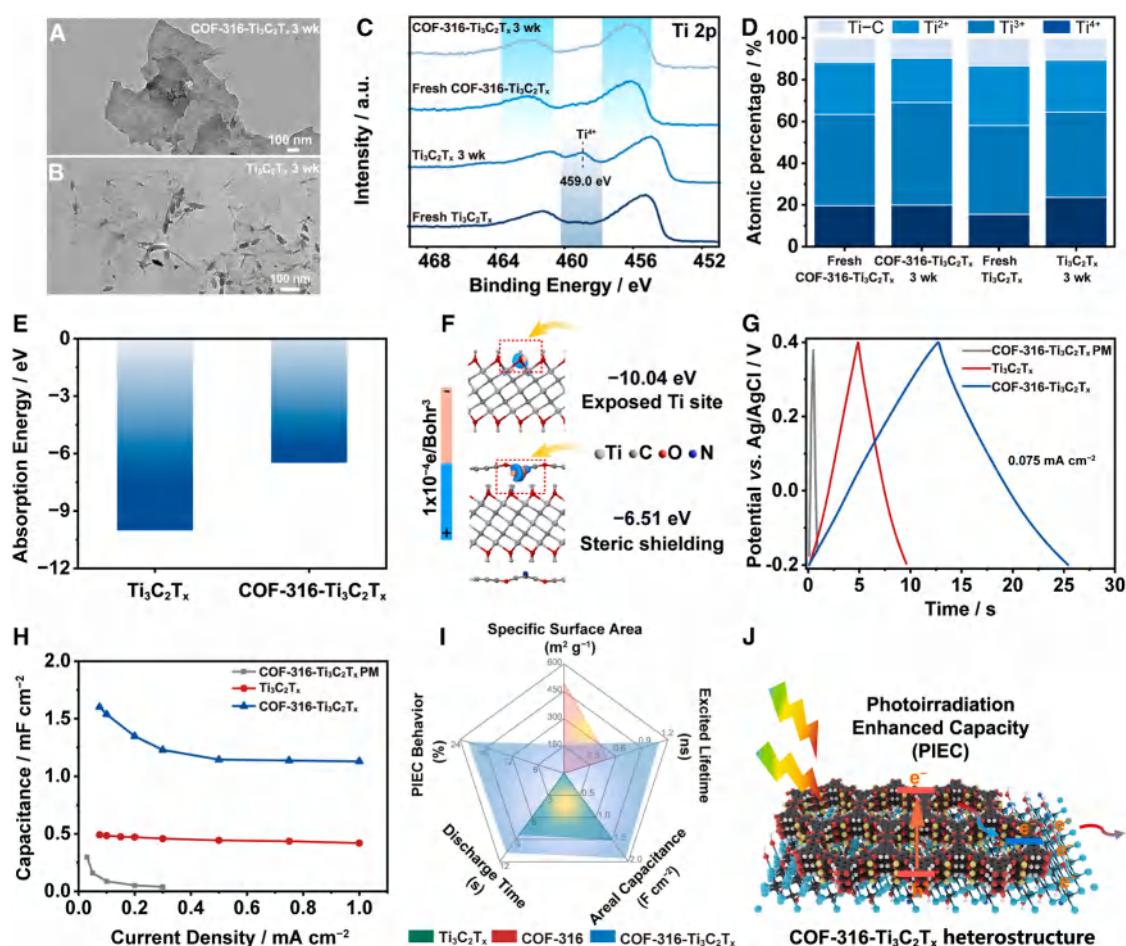


Figure 4. The antioxidant and electrochemical performance characterization of $\text{COF}-316-\text{Ti}_3\text{C}_2\text{T}_x$ electrodes

(A and B) TEM images of $\text{Ti}_3\text{C}_2\text{T}_x$ (A) and $\text{COF}-316-\text{Ti}_3\text{C}_2\text{T}_x$ (B) after being stored in the air for 3 weeks, showing structural stability and morphology retention.

(C and D) Ti 2p spectra and XPS peak fitting results of the Ti 2p regions of $\text{COF}-316-\text{Ti}_3\text{C}_2\text{T}_x$ and $\text{Ti}_3\text{C}_2\text{T}_x$ after 3 weeks, indicating chemical state stability.

(E and F) E_{ad} (E) and $\Delta\rho$ (F) of oxygen radical on different adsorption sites, illustrating oxidation resistance and interfacial charge redistribution. $\Delta\rho$ is calculated by $\Delta\rho = \rho_{o-s} - \rho_o - \rho_s$, where ρ_{o-s} , ρ_o , and ρ_s are the electron density of the oxide, oxygen radical, and oxidized substrate, respectively.

(G and H) GCD curves and C_A of $\text{Ti}_3\text{C}_2\text{T}_x$, $\text{COF}-316-\text{Ti}_3\text{C}_2\text{T}_x$, and $\text{COF}-316-\text{Ti}_3\text{C}_2\text{T}_x$ PM electrodes at different current densities after 3 weeks, demonstrating retention of electrochemical performance.

(I) Radar map of comprehensive properties of $\text{COF}-316$, $\text{Ti}_3\text{C}_2\text{T}_x$, $\text{COF}-316-\text{Ti}_3\text{C}_2\text{T}_x$, highlighting the synergistic advantages of the heterostructure.

(J) Energy storage mechanism of $\text{COF}-316-\text{Ti}_3\text{C}_2\text{T}_x$, showing the roles of charge separation and carrier transport at the interface.

(Figures 5A and 5B). The $\text{COF}-316-\text{Ti}_3\text{C}_2\text{T}_x$ electrode exhibits a clear edge and a regular shape with a width of $650 \mu\text{m}$ and a gap of $350 \mu\text{m}$ through high-precision printing technology, which is conducive to avoiding localized charge concentration and achieving high-density integration in flexible electronic devices (Figure S22). To explore the relative distribution of $\text{COF}-316-\text{Ti}_3\text{C}_2\text{T}_x$ nanosheets in the vertical direction of the electrode, we have investigated the morphology and spatial arrangement using cross-sectional SEM. SEM images indicate that $\text{COF}-316-\text{Ti}_3\text{C}_2\text{T}_x$ nanosheets within the electrode exhibit a compact and interpenetrated stacking morphology, ensuring enhanced mechano-electrochemical stability and electrochemical performance (Figure S23). After bending at arbitrary angles, the corresponding FPMSCs display no visible changes and cracks, showing enhanced flexibility (Figure 5C). The CV curves of

$\text{COF}-316-\text{Ti}_3\text{C}_2\text{T}_x$ FPMSCs exhibit pseudo-rectangular shapes at the scan rates of $3\text{--}1,000 \text{ mV s}^{-1}$, which demonstrates good reversibility and hybrid capacitance of pseudocapacitance and double-layer capacitance (Figure 5D). The GCD curves of $\text{COF}-316-\text{Ti}_3\text{C}_2\text{T}_x$ FPMSCs show a symmetrical nearly triangular shape, which proves supercapacitive characteristics under the charge-discharge process (Figure 5E) and well matches with CV curves.

The PIEC property of $\text{COF}-316-\text{Ti}_3\text{C}_2\text{T}_x$ FPMSCs has been investigated by the variation of their electrochemical performance under light irradiation of simulated solar energy with broadband visible light of $400\text{--}780 \text{ nm}$. To distinguish between heat-only conditions and light-only conditions for accurately understanding the enhancement mechanism, it is necessary to design a series of control experiments with the following

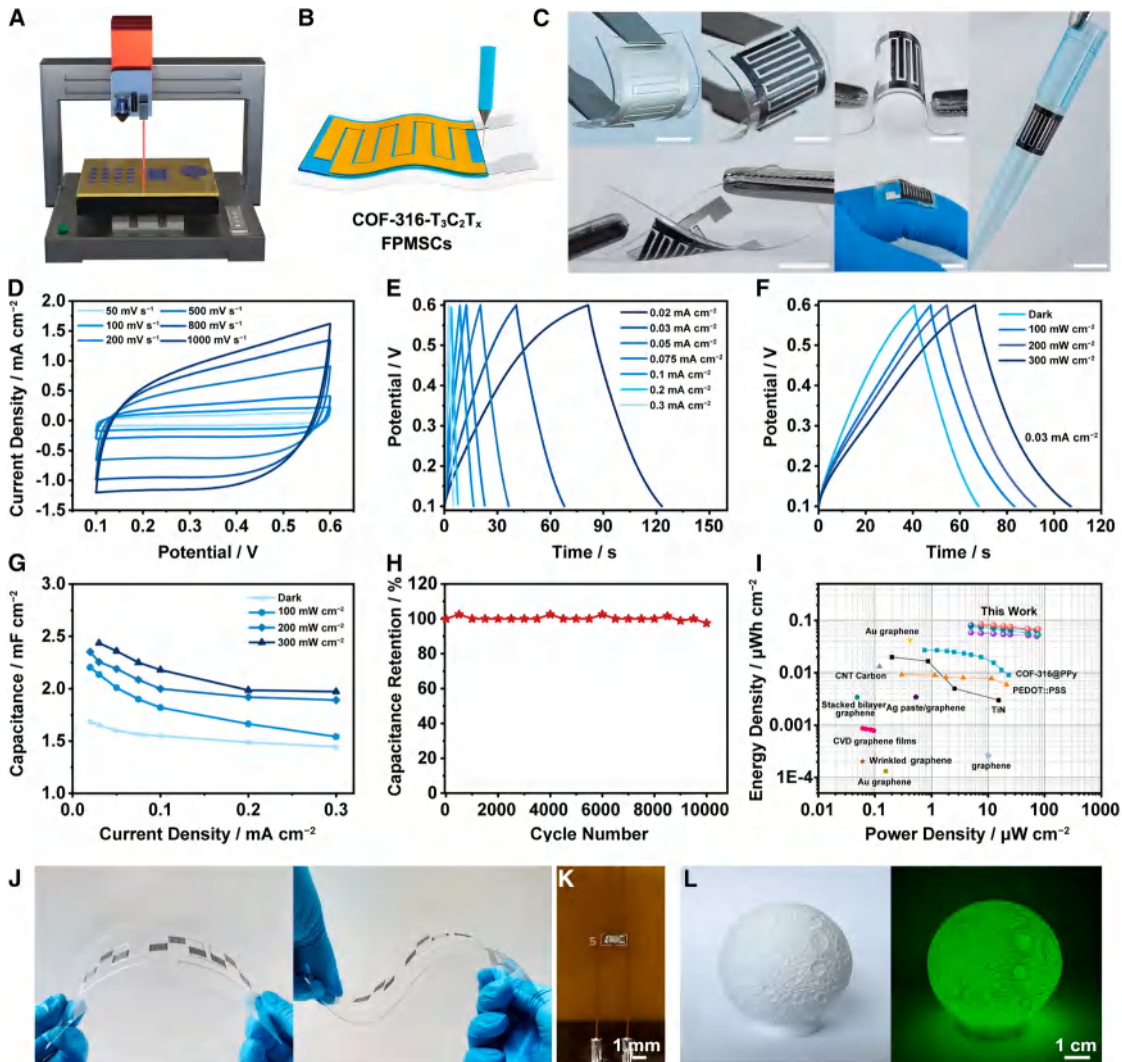


Figure 5. Electrochemical characterization of COF-316-Ti₃C₂T_x FPMSCs

- (A) Diagram depiction of S-SIGMA-CM3-V5 printer.
- (B) Schematic diagram of COF-316-Ti₃C₂T_x FPMSCs, highlighting the device architecture.
- (C) Photograph of COF-316-Ti₃C₂T_x FPMSCs (scan bar: 1 cm), showing device flexibility and uniformity.
- (D) CV curves at different scan rates.
- (E) GCD curves at various current densities, highlighting charge-discharge performance and rate capability.
- (F) GCD curves at 0.03 mA cm⁻² under the photo-radiation power of 300, 200, 100 mW cm⁻², and dark conditions, showing the PIEC behavior.
- (G) C_A is calculated under different photo-radiation powers and dark conditions.
- (H) The cycle stability at 0.02 mA cm⁻², demonstrating long-term electrochemical performance retention.
- (I) Ragone plots of this work and comparison to other reported works, highlighting superior performance.^{47–51}
- (J–L) Photograph of COF-316-Ti₃C₂T_x FPMSCs circuit, green LED circuit, and green LED lighted by COF-316-Ti₃C₂T_x FPMSCs, demonstrating practical energy storage application.

experimental conditions: dark condition (no light); light illumination (400–780 nm, 100 mW cm⁻²); light illumination with cooling condition; heating only (no light, heating the device to 27°C, which is the real-time temperature at the condition of light illumination) (Figures S24–S31).^{52,53} However, the temperature of COF-316-Ti₃C₂T_x FPMSCs rapidly increases and reaches as high as 58°C within a short period under light illumination without any temperature control. It is difficult to obtain reliable electrochemical data under this condition, due to the excessive thermal

accumulation that led to severe thermal degradation and short-circuit failure (Figures S24 and S25). The device temperature is stabilized throughout by employing a cooling system attached to the device to actively regulate the device temperature during light illumination. The GCD curves of COF-316-Ti₃C₂T_x FPMSCs exhibit original shapes and obvious energy storage performance increases under different light irradiation intensities, which reveals that the increased light irradiation intensity has a positive effect on PIEC behavior of COF-316-Ti₃C₂T_x FPMSCs

(Figure 5F). The C_A of COF-316-Ti₃C₂T_x FPMSCs reaches 2.44, 2.26, and 2.14 mF cm⁻² at 300, 200, and 100 mW cm⁻², respectively (Figures S26–S29). The C_A of COF-316-Ti₃C₂T_x FPMSCs under 300 mW cm⁻² is 47.8% higher than that in the dark (1.65 mF cm⁻²). The PIEC effect of COF-316-Ti₃C₂T_x is obvious in the micro-supercapacitors (Figure 5G).

With this cooling system, the device temperature is controlled around 27°C with a slight temperature rise, due to localized heat accumulation. To isolate the influence of temperature from light, the electrochemical performance of the device is investigated under heating-only conditions of 27°C. The corresponding thermal data and energy storage results indicate that the COF-316-Ti₃C₂T_x FPMSCs exhibit a C_A of 1.67 mF cm⁻² under heating-only conditions of 27°C, which is similar to that in the dark of 1.65 mF cm⁻² (Figures S30 and S31). Those results prove that the enhanced energy storage performance mainly originates from PIEC behavior (28.5%) rather than from photo-thermal heating effect (1.5%). The COF-316-Ti₃C₂T_x FPMSCs exhibit a higher C_A than other reported devices (Table S3). They also exhibit a higher PIEC effect than other reported photo-enhanced devices (Table S4). The enhancement in performance can be attributed to the contribution of the COF-316-Ti₃C₂T_x heterointerfaces, which enables synergistic electron-photon harvesting within FPMSCs through the modulation of the built-in electric field.

The COF-316-Ti₃C₂T_x heterostructure demonstrates improvement in antioxidant and structural stability of Ti₃C₂T_x nanosheets to enhance the mechano-electrochemical stability with mechanical flexibility and long-term cycling stability. Both CV curves of COF-316-Ti₃C₂T_x FPMSCs change slightly and exhibit nearly the same C_A (1.47 mF cm⁻²) under various bending states of 0°, 45°, 90°, 120°, 150°, and 180° at 50 mV s⁻¹, which indicates flexibility and lays the foundation for the application of flexible energy storage devices in powering electronic devices (Figure S32). It is worth mentioning that the capacitance retention is 97.5% after 10,000 charge-discharge cycles at 0.2 mA cm⁻² (Figures 5H and S33). To ensure the stability and reliability of the band structure, band structure analysis was carried out using pure COF-316 after the cycling test as an alternative approach. The powder of COF-316 is collected, washed, and subjected to solid-state UV-vis absorption and Mott-Schottky analysis to confirm the band structure (Figures S17 and S18). The results indicate that the band structure of COF-316 remains unchanged before and after testing, demonstrating its stability and reliability. The cycling stability of the device light irradiation is also investigated. The capacitance retention is 93.8% after 5,500 charge-discharge cycles at 0.2 mA cm⁻² under 100 mW cm⁻² (Figure S34), which is mainly caused by the degradation of the solid-state PVA-H₂SO₄ gel electrolyte. It is attributed to the heterostructure improving the structural stability of COF-316-Ti₃C₂T_x composites to endow the device with capacitance retention. Energy density and power density are important parameters to evaluate energy storage devices.⁵⁴ The maximum energy density is 0.085 μWh cm⁻² at a power density of 7.5 μW cm⁻², which indicates an improved performance in comparison with other previously reported devices (Figure 5I).^{47–51} Moreover, the state-of-the-art applications are boosted by storage performance. The actual application can be realized by lighting up a

green LED over 12 s (Figures 5J–5L and S35; Video S1), which promotes the practical potential of COF-316-Ti₃C₂T_x FPMSCs in powering the next-generation of portable flexible electronics.

Conclusions and outlook

We have employed a bonding engineering strategy to synthesize a core-shell COF-316-Ti₃C₂T_x heterostructure, which enables synergistic electron-photon harvesting in FPMSCs through BIEF modulation. The formation mechanism of this core-shell heterostructure is characterized by the preferential surface-initiated dynamic hydrogen bonding anchoring of HHTP monomers that promotes the oriented growth of COF-316 on the surface of Ti₃C₂T_x nanosheets. The core-shell heterostructure suppresses the recombination of photogenerated charges and accelerates interfacial electron transfer, thereby enhancing the PIEC behavior. Additionally, the COF-316-Ti₃C₂T_x FPMSCs achieve an energy density of 0.085 μWh cm⁻² at a power density of 7.5 μW cm⁻², indicating their potential to power flexible devices.

Although primarily designed for flexible photo-assisted supercapacitors with enhanced PIEC performance, the COF/MXene heterostructure exhibits potential for further optimization through interfacial engineering, heteroatom doping, and controlled functional group techniques, broadening its applicability in wearable and adaptive electronics. In addition, expanding the photo-response range via bandgap modulation or integration with multi-energy harvesting systems could further enhance energy conversion efficiency and storage capacity. These developments represent a significant step toward practical, high-performance, and self-sustaining energy storage devices, supporting the advancement of real-world applications for next-generation flexible electronics.

METHODS

Materials

2,3,6,7,10,11-HHTP (>97%) was purchased from Shanghai Tensus Bio-tech. TFPN (98%) was purchased from Energy Chemical Technology. (Shanghai, China). Ti₃AlC₂ bulks (>98 wt %) were purchased from Nanjing Mingshan New Material Technology. (Nanjing, China). Lithium fluoride (LiF) was purchased from Aladdin Chemicals. (Shanghai, China). Polyvinyl alcohol (PVA1799) is purchased from Aladdin Chemicals. (Shanghai, China) N,N-dimethylformamide (DMF), HCl (37%), and H₂SO₄ (98%) were purchased from Lingfeng Industry. (Shanghai, China). Indium tin oxide/polyethylene terephthalate (ITO/PET) was purchased from Yuan Jingmei. (Guangdong, China). All the materials are used as received without further purification.

Synthesis of Ti₃C₂T_x MXene nanosheets

The m-Ti₃C₂T_x was synthesized by selectively etching the Al layer from Ti₃AlC₂ bulk materials. The synthesis commenced with the gradual addition of LiF (0.5 g) to 10 mL of 9 M HCl solution. Afterward, 0.5 g of Ti₃AlC₂ was integrated into the mixture and stirred for 20 min to ensure homogeneity. The solution was then transferred to a Teflon-lined stainless-steel autoclave, where it was heated at 60°C for 24 h to promote the etching process. After cooling, the products were washed six times with deionized water to eliminate residual reagents. The resultant

samples were subsequently dried under vacuum for 12 h. Finally, 100 mg of m-Ti₃C₂T_x was dispersed in 10 mL of deionized water and sonicated for 1 h in an argon atmosphere. The supernatant was collected by centrifugation at 3,500 rpm for 1 h for subsequent applications.

Synthesis of COF-316 electrode

The COF-316 electrode was fabricated by dispersing COF-316 and polyvinylidene fluoride (PVDF) binder in N-methylpyrrolidinone under sonication (150 W, 53 kHz) for 30 min to form a homogeneous slurry. Subsequently, 100 μL of the slurry was drop-cast onto the surface of ITO glass and dried under ambient conditions.

Synthesis of COF-316-Ti₃C₂T_x ink

A homogeneous dispersion was prepared by dissolving 160 mg of COF-316-Ti₃C₂T_x nanosheets in 15 mL of ethylene glycol under continuous stirring (700 rpm, 3 h). The resulting mixture was centrifuged at 5,000 rpm for 1 h to separate the solid phase. After discarding the supernatant, the precipitate was collected as the final ink for subsequent use.

Synthesis of H₂SO₄/PVA gel

One gram of PVA was added to a 25 mL eggplant-shaped bottle, and 10 mL of deionized water was then added under stirring. Following, 0.55 mL of concentrated H₂SO₄ (98%) was added dropwise and stirred evenly. The mixture was then heated at 90°C for 2 h until a transparent gel formed. The H₂SO₄/PVA gel was prepared after cooling.

RESOURCE AVAILABILITY

Lead contact

Requests for further information and resources should be directed to the lead contact, Qiang Zhao (iamqzhao@njupt.edu.cn).

Materials availability

This study did not generate new, unique reagents.

Data and code availability

All data of this study are available within the article and [supplemental information](#).

ACKNOWLEDGMENTS

Weikang Wang and Yan Bai contributed equally to this work. This work was supported by the National Natural Science Foundation of China (62174086, 62474096, 62288102, and 62404113), Basic Research Program of Jiangsu (BK20243057), Outstanding Youth Foundation of Jiangsu Province (BK20240139), Qinglan Project of Jiangsu Province of China, China Postdoctoral Science Foundation (2024M761571), and the Municipal Natural Science Foundation of Qingdao (24-4-4-zrjj-62-jch).

AUTHOR CONTRIBUTIONS

Conceptualization, W.W. and Y.B.; methodology, Z.Y. and P.Y.; interpretation of data and design of platform, W.W., Y.B., N.D., Z.Y., W.Z., P.Y., M.L., S.L., and Q.Z.; manuscript preparation, W.W., Y.B., and N.D.; simulation, N.D.; supervision, W.Z. and Q.Z. All authors edited the manuscript and commented on it.

DECLARATION OF INTERESTS

The authors declare no competing interests.

SUPPLEMENTAL INFORMATION

Supplemental information can be found online at <https://doi.org/10.1016/j.device.2025.100929>.

Received: June 4, 2025

Revised: July 17, 2025

Accepted: August 19, 2025

REFERENCES

- He, J., Cao, L., Cui, J., Fu, G., Jiang, R., Xu, X., and Guan, C. (2024). Flexible energy storage devices to power the future. *Adv. Mater.* 36, 2306090. <https://doi.org/10.1002/adma.202306090>.
- Wang, Y., Sun, X., Liu, Q., and Yu, G. (2025). Functional gel materials for next-generation electrochromic devices and applications. *Chem. Soc. Rev.* 54, 3475–3512. <https://doi.org/10.1039/D4CS01256A>.
- Hua, Q., and Shen, G. (2024). Low-dimensional nanostructures for monolithic 3D-integrated flexible and stretchable electronics. *Chem. Soc. Rev.* 53, 1316–1353. <https://doi.org/10.1039/D3CS00918A>.
- Fox, N. (2023). Increasing solar entitlement and decreasing energy vulnerability in a low-income community by adopting the prosuming project. *Nat. Energy* 8, 74–83. <https://doi.org/10.1038/s41560-022-01169-5>.
- Xu, Y., Ai, S., Wu, T., Zhou, C., Huang, Q., Li, B., Tian, D., and Bu, X.H. (2025). Bioinspired photo-thermal catalytic system using covalent organic framework-based aerogel for synchronous seawater desalination and H₂O₂ production. *Angew. Chem. Int. Ed.* 64, e202421990. <https://doi.org/10.1002/anie.202421990>.
- Wang, Z., Hölzel, H., Fernandez, L., Aslam, A.S., Baronas, P., Orrego Hernández, J., Ghasemi, S., Campoy Quiles, M., and Moth Poulsen, K. (2024). Hybrid solar energy device for simultaneous electric power generation and molecular solar thermal energy storage. *Joule* 8, 2607–2622. <https://doi.org/10.1016/j.joule.2024.06.012>.
- Liang, S., Zheng, L.J., Song, L.N., Wang, X.X., Tu, W.B., and Xu, J.J. (2024). Manipulation of neural progenitor fate through the oxygen sensing pathway. *Adv. Mater.* 36, 2307790. <https://doi.org/10.1002/adma.202307790>.
- An, C., Wang, Z., Xi, W., Wang, K., Liu, X., and Ding, Y. (2019). Nanoporous Cu@Cu₂O hybrid arrays enable photo-assisted supercapacitor with enhanced capacities. *J. Mater. Chem. A* 7, 15691–15697. <https://doi.org/10.1039/C9TA03707A>.
- Bai, L., Huang, H., Zhang, S., Hao, L., Zhang, Z., Li, H., Sun, L., Guo, L., Huang, H., and Zhang, Y. (2020). Photocatalysis-assisted Co₃O₄/g-C₃N₄ p–n junction all-solid-state supercapacitors: A bridge between energy storage and photocatalysis. *Adv. Sci.* 7, 2001939. <https://doi.org/10.1002/advs.202001939>.
- Wijesundara, Y.H., Howlett, T.S., Kumari, S., and Gassensmith, J.J. (2024). The promise and potential of metal–organic frameworks and covalent organic frameworks in vaccine nanotechnology. *Chem. Rev.* 124, 3013–3036. <https://doi.org/10.1021/acs.chemrev.3c00409>.
- Zhao, W., Zhu, Q., Wu, X., and Zhao, D. (2024). The development of catalysts and auxiliaries for the synthesis of covalent organic frameworks. *Chem. Soc. Rev.* 53, 7531–7565. <https://doi.org/10.1039/D3CS00908D>.
- Chu, X., Liu, S., Luan, B.B., Zhang, Y., Xi, Y., Shao, L.H., Zhang, F.M., and Lan, Y.Q. (2025). Crystal-facet-controlled internal electric field in MOF/COF heterojunction towards efficient photocatalytic overall water splitting. *Angew. Chem. Int. Ed.* 64, e202422940. <https://doi.org/10.1002/anie.202422940>.

13. Chen, Y.F., Fang, Y., Zhu, N.N., Luo, X., Zhu, G.Y., Yang, M., Chen, R.H., Zeng, X., Xiao, J.M., Liu, L., et al. (2025). Multi-shelled hollow covalent organic framework nanospheres for stable potassium storage. *Angew. Chem. Int. Ed.* 64, e202424641. <https://doi.org/10.1002/anie.202424641>.
14. Cao, J., Ji, Y., and Shao, Z. (2024). Nanotechnologies in ceramic electrochemical cells. *Chem. Soc. Rev.* 53, 450–501. <https://doi.org/10.1039/D3CS00303E>.
15. Lu, X., Zhang, K., Niu, X., Ren, D.D., Zhou, Z., Dang, L.L., Fu, H.R., Tan, C., Ma, L., and Zang, S.Q. (2024). Encapsulation engineering of porous crystalline frameworks for delayed luminescence and circularly polarized luminescence. *Chem. Soc. Rev.* 53, 6694–6734. <https://doi.org/10.1039/D3CS01026K>.
16. Wen, G., Sun, L., Qin, Y., Liu, S., Ma, L., Zhang, N., Liu, S., Yin, Y., Ren, B., and Wang, S. (2025). COF-assisted construction of steric mass-charge channels to boost activity for high-performance fuel cells. *Angew. Chem. Int. Ed.* 64, e202424179. <https://doi.org/10.1002/anie.202424179>.
17. Xia, Y., Zhang, W., Yang, S., Wang, L., and Yu, G. (2023). Research progress in donor-acceptor type covalent organic frameworks. *Adv. Mater.* 35, 2301190. <https://doi.org/10.1002/adma.202301190>.
18. He, Z., Luan, T., Wei, Q., Wang, L., Huang, D., Chen, H., Yu Dmitriev, I., Li, P., Zhang, S., and Yu, W.W. (2025). Metalized porphyrin-based COFs for conductive porous layers in perovskite solar cells to enhance electron injection, defect passivation, and lead-protection. *Angew. Chem. Int. Ed.* 64, e202505470. <https://doi.org/10.1002/anie.202505470>.
19. Zhou, T., Ma, Y., Feng, H., Lu, Y., Che, G., Liu, C., and Lan, Y. (2024). COFs-based metal-free heterojunctions for solar-to-chemical energy conversion. *Adv. Funct. Mater.* 34, 2409396. <https://doi.org/10.1002/adfm.202409396>.
20. Guo, Q., Ji, D., Wang, Q., Peng, L., Zhang, C., Wu, Y., Kong, D., Luo, S., Liu, W., Chen, G., et al. (2024). Supercapacitively liquid-solid dual-state optoelectronics. *Adv. Mater.* 36, 2406345. <https://doi.org/10.1002/adma.202406345>.
21. Wang, H., Qian, C., Liu, J., Zeng, Y., Wang, D., Zhou, W., Gu, L., Wu, H., Liu, G., and Zhao, Y. (2020). Integrating suitable linkage of covalent organic frameworks into covalently bridged inorganic/organic hybrids toward efficient photocatalysis. *J. Am. Chem. Soc.* 142, 4862–4871. <https://doi.org/10.1021/jacs.Oc00054>.
22. Qin, R., Nong, J., Wang, K., Liu, Y., Zhou, S., Hu, M., Zhao, H., and Shan, G. (2024). Recent advances in flexible pressure sensors based on MXene materials. *Adv. Mater.* 36, 2312761. <https://doi.org/10.1002/adma.202312761>.
23. Guo, J., Ma, G., Liu, G., Dai, C., and Lin, Z. (2024). Ti₂CT MXene cathode host for enhanced zinc-bromine battery performance. *Adv. Energy Mater.* 14, 2304516. <https://doi.org/10.1002/aenm.202304516>.
24. Hu, Y., Cai, J., Shen, G., Zhao, Z., Liu, Y., Liu, S., Tu, S., Tian, Y., Lu, H., Wang, J., et al. (2025). Selective hydrogenolysis of biomass-derived aromatic alcohols over 2D-Mo₂CO_x MXene by a reversible redox-relay mechanism. *Angew. Chem. Int. Ed.* 64, e202500881. <https://doi.org/10.1002/anie.202500881>.
25. Ponnalagar, D., Hang, D.R., Liang, C.T., and Chou, M.M.C. (2024). Recent advances and future prospects of low-dimensional Mo₂C MXene-based electrode for flexible electrochemical energy storage devices. *Prog. Mater. Sci.* 145, 101308. <https://doi.org/10.1016/j.jpmatsci.2024.101308>.
26. Natu, V., Hart, J.L., Sokol, M., Chiang, H., Taheri, M.L., and Barsoum, M.W. (2019). Edge capping of 2D-MXene sheets with polyanionic salts to mitigate oxidation in aqueous colloidal suspensions. *Angew. Chem. Int. Ed.* 58, 12655–12660. <https://doi.org/10.1002/anie.201906138>.
27. Zhang, L., Li, H., Zhang, X., Liu, C., Sun, Y., Zhang, Y., Fang, Z., He, J., Wang, R., Jiang, K., and Chen, D. (2025). Ultra-rapid synthesis of high-entropy MAX phases and their derivative MXenes for battery electrodes. *Angew. Chem. Int. Ed.* 64, e202418538. <https://doi.org/10.1002/anie.202418538>.
28. Liu, N., Li, Q., Wan, H., Chang, L., Wang, H., Fang, J., Ding, T., Wen, Q., Zhou, L., and Xiao, X. (2022). High-temperature stability in air of Ti₃C₂T_x MXene-based composite with extracted bentonite. *Nat. Commun.* 13, 5551. <https://doi.org/10.1038/s41467-022-33280-2>.
29. Li, Z., Liu, C., Deng, Q., and Deng, W. (2024). Rational design of covalent organic frameworks as photocatalysts for water splitting. *Adv. Funct. Mater.* 34, 2402676. <https://doi.org/10.1002/adfm.202402676>.
30. Wang, F., Tian, F., Xia, X., Pang, Z., Wang, S., Yu, X., Li, G., Zhao, Y., Xu, Q., Hu, S., et al. (2024). One-step synthesis of organic terminal 2D Ti₃C₂T_x MXene nanosheets by etching of Ti₃AlC₂ in an organic lewis acid solvent. *Angew. Chem. Int. Ed.* 63, e202405315. <https://doi.org/10.1002/anie.202405315>.
31. Zhang, B., Wei, M., Mao, H., Pei, X., Alshimiri, S.A., Reimer, J.A., and Yaghi, O.M. (2018). Crystalline dioxin-linked covalent organic frameworks from irreversible reactions. *J. Am. Chem. Soc.* 140, 12715–12719. <https://doi.org/10.1021/jacs.Bb08374>.
32. Guan, X., Li, H., Ma, Y., Xue, M., Fang, Q., Yan, Y., Valtchev, V., and Qiu, S. (2019). Chemically stable polyarylether-based covalent organic frameworks. *Nat. Chem.* 11, 587–594. <https://doi.org/10.1038/s41557-019-0238-5>.
33. Zhao, X., Chen, Y., Niu, R., Tang, Y., Chen, Y., Su, H., Yang, Z., Jing, X., Guan, H., Gao, R., and Meng, L. (2024). Nir plasmonic nanozymes: Synergistic enhancement mechanism and multi-modal anti-infection applications of MXene/MOFs. *Adv. Mater.* 36, 2307839. <https://doi.org/10.1002/adma.202307839>.
34. Qin, M., Zhang, X., Ding, H., Chen, Y., He, W., Wei, Y., Chen, W., Chan, Y.K., Shi, Y., Huang, D., and Deng, Y. (2024). Engineered probiotic bio-heterojunction with robust antibiofilm modality via “eating” extracellular polymeric substances for wound regeneration. *Adv. Mater.* 36, 2402530. <https://doi.org/10.1002/adma.202402530>.
35. Wang, H., Jiang, H., Niu, Y., Siddiqui, N.A., Khan, A., Pan, L., and Lin, J. (2025). Three-dimensional structured of V-doped CoP in situ grown on MXene as highly efficient bifunctional electrocatalyst for water splitting. *Nano Res.* 18, 94907238. <https://doi.org/10.26599/NR.2025.94907238>.
36. Yang, J., Shi, F., Zhou, C., Zhang, S., Sui, Q., and Chen, L. (2024). Machine learning and theoretical prediction of highly spin-polarized Cr₂CO MXene with enhanced curie temperature. *Adv. Funct. Mater.* 34, 2411170. <https://doi.org/10.1002/adfm.202411170>.
37. Liu, D., Liu, Z., Gao, X., Zhu, J., Wang, Z., Qiu, R., Ren, Q., Zhang, Y., Zhang, S., and Zhang, M. (2024). Hydrogen-bonding integrated low-dimensional flexible electronics beyond the limitations of van der waals contacts. *Adv. Mater.* 36, 2404626. <https://doi.org/10.1002/adma.202404626>.
38. Wang, X., Wang, Y., Ma, M., Zhao, X., Zhang, J., and Zhang, F. (2024). P-N bonds-mediated atomic-level charge-transfer channel fabricated between violet phosphorus and carbon nitride favors charge separation and water splitting. *Small* 20, 2311841. <https://doi.org/10.1002/smll.202311841>.
39. Zhao, W., Peng, J., Wang, W., Jin, B., Chen, T., Liu, S., Zhao, Q., and Huang, W. (2019). Interlayer hydrogen-bonded metal porphyrin frameworks/MXene hybrid film with high capacitance for flexible all-solid-state supercapacitors. *Small* 15, 1901351. <https://doi.org/10.1002/smll.201901351>.
40. Li, Y., Zhang, J., Chen, Q., Xia, X., and Chen, M. (2021). Emerging of heterostructure materials in energy storage: A review. *Adv. Mater.* 33, 2100855. <https://doi.org/10.1002/adma.202100855>.
41. Zhu, Y., Deebansok, S., Deng, J., Wang, X., Brousse, T., Favier, F., and Fontaine, O. (2024). Electron delocalization and electrochemical potential distribution phenomena in faradaic electrode materials for understanding electrochemical behavior. *Adv. Energy Mater.* 14, 2304317. <https://doi.org/10.1002/aenm.202304317>.
42. Gong, G., Liu, Y., Mao, B., Tan, L., Yang, Y., and Shi, W. (2017). Ag doping of Zn-In-S quantum dots for photocatalytic hydrogen evolution: simultaneous bandgap narrowing and carrier lifetime elongation. *Appl. Catal. B Environ.* 216, 11–19. <https://doi.org/10.1016/j.apcatb.2017.05.050>.

43. Wu, Y., Hu, Q., Liang, H., Wang, A., Xu, H., Wang, L., and He, X. (2023). Electrostatic potential as solvent descriptor to enable rational electrolyte design for lithium batteries. *Adv. Energy Mater.* 13, 2300259. <https://doi.org/10.1002/aenm.202300259>.
44. Chen, Z., Wang, J., Hao, M., Xie, Y., Liu, X., Yang, H., Waterhouse, G.I.N., Wang, X., and Ma, S. (2023). Tuning excited state electronic structure and charge transport in covalent organic frameworks for enhanced photocatalytic performance. *Nat. Commun.* 14, 1106. <https://doi.org/10.1038/s41467-023-36710-x>.
45. Lu, J.N., Liu, J.J., Dong, L.Z., Lin, J.M., Yu, F., Liu, J., and Lan, Y.Q. (2023). Synergistic metal-nonmetal active sites in a metal-organic cage for efficient photocatalytic synthesis of hydrogen peroxide in pure water. *Angew. Chem. Int. Ed.* 62, e202308505. <https://doi.org/10.1002/anie.202308505>.
46. Schulte, F.K. (1976). A theory of thin metal films: Electron density, potentials and work function. *Surf. Sci.* 55, 427–444. [https://doi.org/10.1016/0039-6028\(76\)90250-8](https://doi.org/10.1016/0039-6028(76)90250-8).
47. Delekta, S.S., Smith, A.D., Li, J., and Östling, M. (2017). Inkjet printed highly transparent and flexible graphene micro-supercapacitors. *Nanoscale* 9, 6998–7005. <https://doi.org/10.1039/C7nr02204b>.
48. Chen, T., Xue, Y., Roy, A.K., and Dai, L. (2014). Transparent and stretchable high-performance supercapacitors based on wrinkled graphene electrodes. *ACS Nano* 8, 1039–1046. <https://doi.org/10.1021/nn405939w>.
49. Xu, P., Kang, J., Choi, J.B., Suhr, J., Yu, J., Li, F., Byun, J.H., Kim, B.S., and Chou, T.W. (2014). Laminated ultrathin chemical vapor deposition graphene films based stretchable and transparent high-rate supercapacitor. *ACS Nano* 8, 9437–9445. <https://doi.org/10.1021/nm503570j>.
50. Zhong, Y., Zhang, X., He, Y., Peng, H., Wang, G., and Xin, G. (2018). Simultaneously armored and active graphene for transparent and flexible supercapacitors. *Adv. Funct. Mater.* 28, 1801998. <https://doi.org/10.1002/adfm.201801998>.
51. Jo, K., Lee, S., Kim, S.M., In, J.B., Lee, S.M., Kim, J.H., Lee, H.J., and Kim, K.S. (2015). Stacked bilayer graphene and redox-active interlayer for transparent and flexible high-performance supercapacitors. *Chem. Mater.* 27, 3621–3627. <https://doi.org/10.1021/cm504801r>.
52. Yang, K., Fu, H., Duan, Y., Ma, Z., Wang, D., Li, B., Park, H.S., and Ho, D. (2024). Poloxamer pre-solvation sheath ion encapsulation strategy for zinc anode-electrolyte interfaces. *ACS Energy Lett.* 9, 209–217. <https://doi.org/10.1021/acsenergylett.3c02337>.
53. Pujari, A., Shimokawa, K., and De Volder, M. (2025). Photobatteries: Prospects and fundamental limitations. *Joule* 9, 2542–4785. <https://doi.org/10.1016/j.joule.2025.101869>.
54. Bai, Y., Shen, B., Zhang, S., Zhu, Z., Sun, S., Gao, J., Li, B., Wang, Y., Zhang, R., and Wei, F. (2019). Storage of mechanical energy based on carbon nanotubes with high energy density and power density. *Adv. Mater.* 31, 1800680. <https://doi.org/10.1002/adma.201800680>.